High-resolution X-ray computed tomography simulations of synthetically-generated volume porosity in continuous carbon fibre-reinforced polymer samples

Bernhard Plank, Markus G. R. Sause, Johann Kastner

Angaben zur Veröffentlichung / Publication details:

Plank, Bernhard, Markus G. R. Sause, and Johann Kastner. 2022. "High-resolution X-ray computed tomography simulations of synthetically-generated volume porosity in continuous carbon fibre-reinforced polymer samples." Nondestructive Testing and Evaluation 37 (5): 645–65.
https://doi.org/10.1080/10589759.2022.2086547.

High-resolution X-ray computed tomography simulations of synthetically-generated volume porosity in continuous carbon fibre-reinforced polymer samples

Bernhard Plank [a,b], Markus G. R. Sause [b] and Johann Kastner [a]

[a]Research Group Computed Tomography, University of Applied Sciences Upper Austria, Wels, Austria; [b]Institute of Materials Resource Management, University of Augsburg, Augsburg, Germany

ABSTRACT

The fast and correct determination of porosity in carbon fibre–reinforced polymers and other polymeric material is an important application area of X-ray computed tomography (CT). In this CT simulation study, microstructures such as individual carbon fibres, micro-voids, as well as the polymer matrix including mesoscale voids, were taken into account to generate CT data synthetically with well-known porosity. It was found that the ratio of total surface area (SA) of the voids divided by the total volume (V) of the voids is suitable to describe and differentiate individual porosity samples. Our investigations revealed that the ratio SA/V can be used to estimate a minimal necessary voxel size for proper porosity segmentation by a simple ISO50 threshold. Under certain conditions, using an adapted ISOxx threshold value at a resolution of $(10\ \mu m)^3$ voxel size, the porosity in a specimen can be determined with an average measurement error below 10%. As long as the CT resolution is not high enough to completely resolve all void structures, using global threshold segmentation is always a compromise between over-segmentation of the macro-voids and under-segmentation of micro-voids.

1. Introduction

In modern lightweight construction in many areas, such as the aerospace and automotive industries, a wide variety of material combinations are used for fibre-reinforced composite systems. Due to their excellent mechanical properties, carbon fibre–reinforced polymers (CFRP) are much used in industry, especially for highly stressed structural components. The increasing use of CFRP for safety-critical products requires strict quality control evaluation techniques [1]. A main manufacturing problem for CFRP is that many bubbles filled with gas or air [2,3] are trapped in the polymer matrix, known as porosity. Voids can also be induced by residual volatiles and moisture [4]. Typically, microbubbles are located between the individual carbon fibres, and meso- or macropores are found between the fibre bundles in polymer-rich regions. [5,6] A high degree of porosity can critically weaken the material strength [7], and the interlaminar shear strength can be reduced significantly in CFRP [8,9] by the presence of voids.

CONTACT Bernhard Plank Bernhard.Plank@fh-wels.at

In aerospace, currently classic epoxy–resin systems with additional additives are mostly used, but thermoplastics such as polyamides or PEEK are increasingly being used as matrix systems due to the improved automation capabilities required for future mass production lines. Especially, the development of new additive manufacturing methods, such as selective laser sintering (SLS) [10] or fused deposition modelling (FDM) [11], needs reliable quality control of the inner highly complex microstructures to guarantee the required mechanical properties. Porosity should be determined as accurately as possible, especially for typical industrial porosity tolerances in the range of <2.5 vol.% [12]. However, the standard measurement methods currently used, such as standardised thermo-chemical analysis (DIN EN 2564:1998), provide relatively poor accuracy of about ±1.0 vol.% or even significantly lower. In addition, no information about three-dimensional microstructures is given, and the specimens will be destroyed completely during the porosity analysis.

Therefore, investigations with X-ray computed tomography (CT) can show relevant information about the inner microstructures of products with high accuracy compared to the mentioned standard method for porosity determination of CFRPs. This high accuracy of CT has a disadvantage in practice: it is almost impossible to obtain suitable 3D data with precisely defined porosities directly from a CT scan, as the production of exact CFRP reference components that have a high number of well-defined micropores below 10 µm is almost impossible. Reference samples [13] with void-like structures in the range of >200 µm give only a good impression of the capability of CT for meso- and macro-voids. Furthermore, it is impossible to produce accurate reference samples for all the above material combinations, as their different X-ray absorption properties significantly affect the CT results and thus the final porosity evaluation. Nevertheless, the reproducibility for evaluations of the same specimens by means of CT is very high, with errors below 1% [14].

Recent studies have shown the high potential of performing CT simulations to generate very well-described 3D data with well-known internal structures [15]. Due to the high computational complexity, individual fibres were usually not considered for modelling porosity in fibre-reinforced polymers, as well as micro-porosity between individual carbon fibres [12,16,17].

In order to obtain a more realistic and complex grey value distribution in the CT simulation data, typical microstructures such as single fibres, needle-shaped micro-pores in the fibre bundles and meso- and macro-pores are taken into account in this work, as well different polymer matrix systems. These complex models should lead to a better understanding of quantitative porosity evaluation using CT. The aim of this research is to provide values for the uncertainty of the segmentation results using an easy-to-implement and customisable thresholding procedure [13].

2. Materials and methods

2.1. CT simulations

For the high-resolution CT simulations, a software tool called ‘SimCT’ developed by M. Reiter [15,18] was used in this study. This software tool allows numerical simulation of CT systems, including X-ray physics and artefact mechanisms in order of the chosen CT and material parameters. It includes the entire process chain of a typical CT scan, starting

from X-ray generation, interactions of X-rays within specimens and X-ray detection in a detector, while considering the most relevant physical effects (PEs) [18]. Most relevant PEs to be considered were detector and photon noise to provide realistic noise contribution and image blur caused by the scintillator [19]. Propagation-based phase contrast effects [20] are not implemented in the SimCT tool.

As a numerical input, a *.geo text-file was semi-automatically generated, containing all relevant information about the used artificial specimen. In these generated *.geo files, individual elements were used, each of them represented by an assigned material defined by mass-weighted molecular formulae plus density values as well as defined surface type. The element surface is described by simple geometries such as cuboid, cylindrical, conical or ellipsoidal calculated in SimCT tool by mathematical equations. Altogether, a small cut-out of a typical fibre-reinforced polymer cube with a sample volume of 0.375^3 mm^3 is mathematically described, including fibre roving, with individual carbon fibres orientated in 0 and 90° containing needle-like micro-voids as well as one large polymer–matrix volume containing macro-voids. To avoid periodical structures, all individual fibres and micro-voids have a random position and a random elliptical shape, resulting in a minor and major diameter variation of the C-fibres between 5.8 and 6.2 µm as well 3 and 13.5 µm for the micro-voids. The minor and major ellipsoidal dimensions of the manual modelled meso- and macro-voids range from 2.5 to 200 µm. Altogether, the used artificial CFRP specimen in this study is mathematically descripted by 1,988 different elements in the input file. As fibres, C-fibres with a density of 1.75 g/cm^3, as pores, air at 20°C with 0.0012 g/cm^3 and two different polymer–matrix materials, epoxy resin (1.36 g/cm^3) and thermoplastic polyamide 6 (1.13 g/cm^3), were defined. The CT simulations were done by using a tube model of a 160 kV nano-focus X-ray tube from Hamamatsu and a detector model of a Varian flat panel detector. Both tube and detector are also used in the real-world nano-CT systems such as the EasyTom 160 from RX Solutions [18]. Using a tube voltage of 60 kV for this study, simulations with voxel sizes between $(0.5\ \mu m)^3$ and $(40\ \mu m)^3$, as well as with and without enabled physical effects, were performed to create data with typical CT measurement artefacts and image noise. These enabled physical effects are photon and Gaussian noise, focal spot Gaussian blur and detector modulation transfer function (MTF), usually occurring during real CT scans. Dependent on the voxel size and therefore the required amount of detector pixels to be simulated, one projection image takes between 130 s $(0.5\ \mu m)^3$ and 1.4 s $(40\ \mu m)^3$ calculation time on an actual workstation. This multiplied by 1440 projections, which were used for the $(0.5\ \mu m)^3$ dataset, results in a maximum calculation time of 52 h for one 3D dataset of 1280^3 voxels.

Figure 1(a) represents a 3D visualization of the voids used for further porosity evaluation. In Figure 1(b), one-slice image of the binarised input model is visualised,depicting the individual C-fibres orientated in 0 and 90° in white, the polymer matrix between the individual C-fibres and a neat polymer–matrix cluster inbright-grey, as well as needle-like micro- and elliptical/spherical meso- and macro-voids in dark-grey colour. In Figure 1(c), a simulation of an ideal CT scan of the CFRP specimen is shown, performed at $(0.5\ \mu m)^3$ voxel size and with disabled physical effects. For Figure 1(d-f), physical effects were enabled. The difference in contrast of the polymer-rich areas compared to the C-fibres is explained by different polymer material models used here. For Figure 1(f), epoxy resin (1.36 g/cm^3), for Figure 1(e), polyamide 6 (1.13 g/cm^3) and forFigure 1(d), epoxy resin plus sulphur

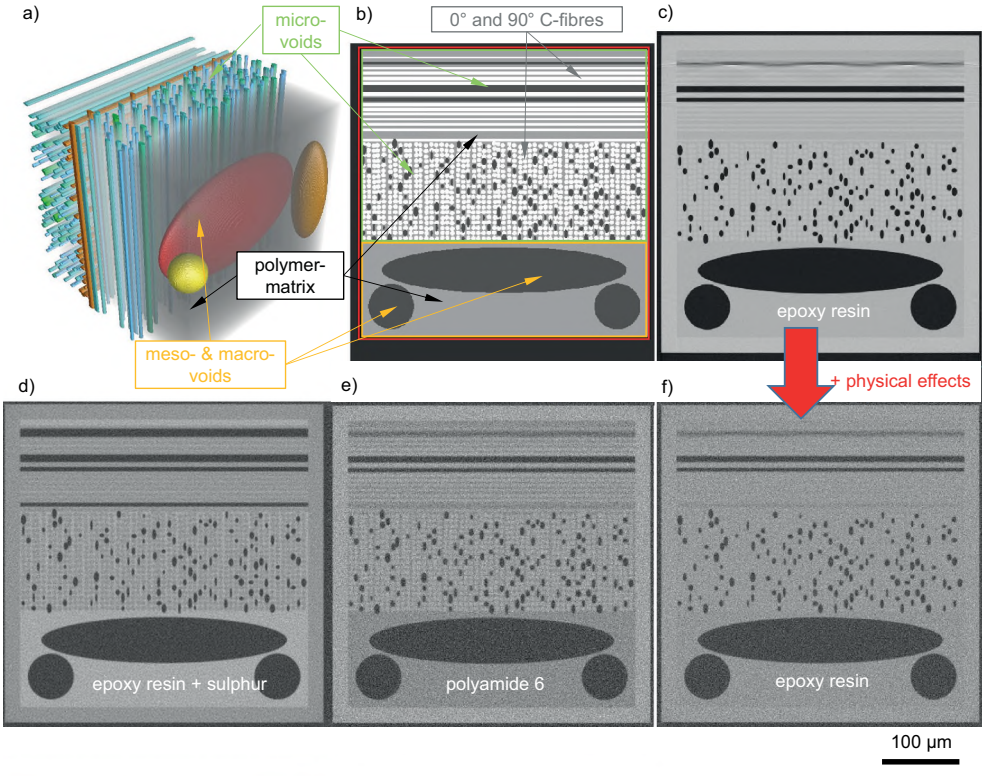

Figure 1. 3D view of segmented micro- and macro-voids (a) as well as one binary axial slice image (b) without any physical effects. CT simulation slice images performed at $(0.5\ \mu m)^3$ voxel size are shown in (c)–(e), whereas in (d)–(f), additional physical effects such as noise and image blur caused by the scintillator were enabled in the SimCT tool. For (d), epoxy resin + sulphur (1.31 g/cm^3), for (e), polyamide 6 (1.13 g/cm^3) and for (c and f), epoxy resin (1.36 g/cm^3) was used as the polymer material model.

(1.31g/cm^3), simulating additional typical additives in polymers, was used for CT simulations. To avoid edge-effects and segmentation errors with the surrounding air at lower resolutions, an additional border of carbon (1.75 g/cm^3) was modelled in the final simulation study Figure 1(c-f). In Figure 2(a), the resulting grey value histograms of Figure 1(c,f) are shown, showing how important enabled physical effects are to deliver a realistic grey value distribution, whereas typically the C-fibres cannot be distinguished from the epoxy resin [14].

2.2. ISOxx thresholding and segmentation

As mentioned in the introduction of this paper, this study was mainly conducted to test a simple and reproducible threshold method. As an abbreviation, it is named 'ISOxx' in the following manuscript. The ISOxx method is usually very fast, even with large data sets, and can be easily calculated, adapted and applied with most available software tools [13]. This ISOxx threshold is typically calculated from the grey value histogram as shown in Figure 2(b) by Equation (1):

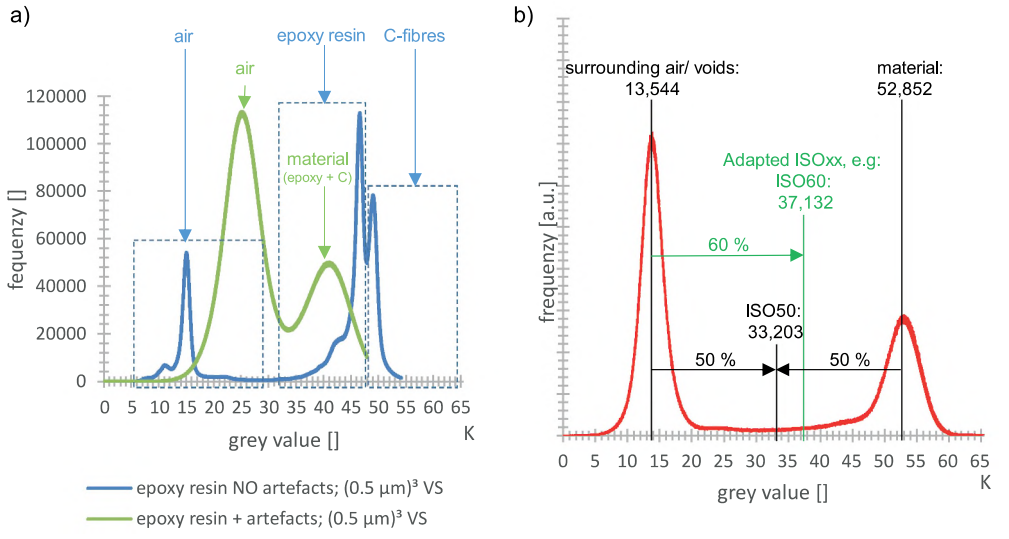

Figure 2. (A) Grey value histogram from simulation data shown in Figure 1(c) and (f) with and without enabled physical effects (artefacts). (b) Grey value histogram-based calculation of an ISOxx threshold for porosity segmentation. Units of the grey values in thousands (K) of typical 16-bit image datasets.

$$ISO_{threshold} = Peak_{Air} + \frac{(Peak_{Material} - Peak_{Air}) * ISOxx}{100} \quad (1)$$

where the positions of the material peak ($Peak_{Material}$) and the voids, respectively, surrounding air ($Peak_{Air}$) is taken into account. Therefore, an ISOxx value of 50% (ISO50) calculates the mid-point grey value between the material and air peak. With this calculated $ISO_{threshold}$ the segmentation of all voxels below this value can be carried out to calculate the porosity (Φ) by a ratio of 'segmented Voxels/total Voxels' in a defined region of interest (ROI).

Data handling, registration, as well as the definition of the relevant region of interest (ROIs), the calculation of the ISOxx threshold and void segmentation were done in the commercial software tool VG Studio Max 3.4 (Volumegraphics GmbH., Heidelberg, Germany) using the 'surface determination tool' as well the 'Porosity/Inclusion tool – only threshold'. All filters were disabled, except using a 'minimal voxel size' of 8 for segmentation, to reduce possible over-segmentation of noisy voxels.

3. Results and discussion

3.1. Image quality analysis

In Figure 3, a comparison between simulation results without and with enabled physical effects (+PE) at different voxel size for the epoxy resin specimen is shown. In addition, the grey values of a line profile (green line) involving neat epoxy resin, a macro/meso-void and a micro-void is depicted. Corresponding grey values are shown in Figure 4.

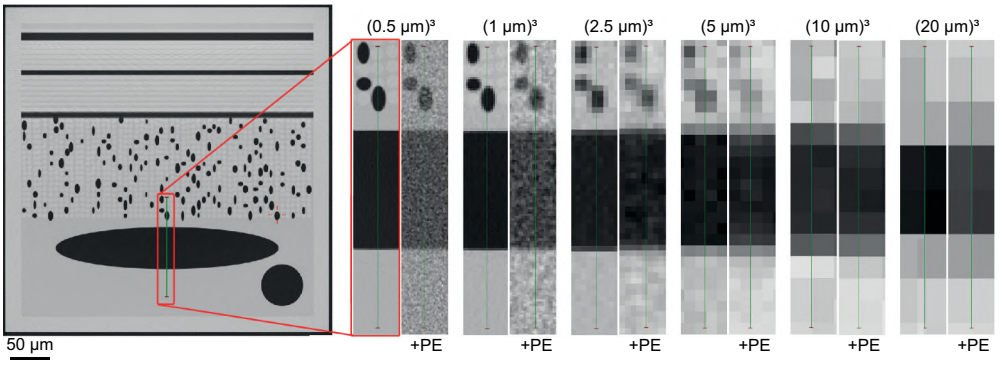

Figure 3. Simulation results with disabled (noPE) and with enabled physical effects (+PE) at various voxel sizes for the epoxy resin specimen. Green line indicates the position of the line profiles for grey value evaluation shown in Figure 4.

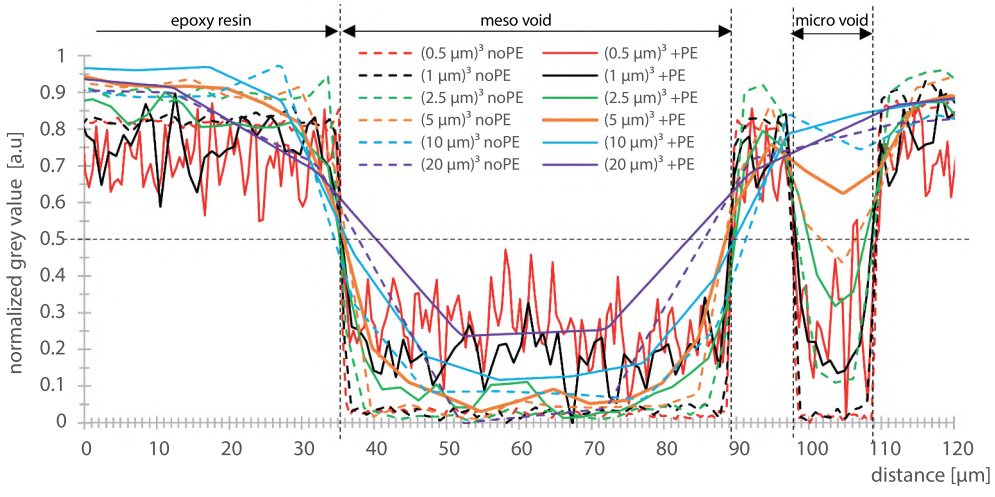

Figure 4. Normalized grey values along the defined line profile from Figure 3 with disabled (noPE) and with enabled physical effects (+PE) at various voxel sizes for the epoxy resin specimen.

In Figure 4, grey value line profiles crossing the boundary from neat epoxy-rich regions to a macro-/meso-void and a micro-void are shown, depicting the results on different voxel sizes and the impact of enabled physical effects. For better comparison, for each line profile, the grey values were normalised to the maximum and minimum available grey value. As soon PE are enabled, for high-resolution CT simulations in the range of $(0.5\ \mu m)^3$ and $(1\ \mu m)^3$, strong image noise occurs. At voxel size above $(2.5\ \mu m)^3$, noise significantly reduced. In addition, the line profiles show that the meso-void located at a distance between 35 and 90 µm can be clearly distinguished. The shown micro-void located at a distance between 98 and 109 µm can only be clearly distinguished up to a voxel size of $(2.5\ \mu m)^3$, using a threshold of 0.5 normalised grey values. In addition in the

micro void at a distance of 107 µm, the $(0.5\ \mu m)^3$ +PE line profile exceeds a normalised grey value of 0.5 due to high image noise. This would lead to an under-segmentation of the micro-void using an ISO50 threshold for this region.

To quantify the image noise, a contrast to noise ratio (CNR) according to ISO 15,708-2:2017 [21] Equation (2) was calculated:

$$\mathrm{CNR} = \frac{\left|\mu_{epoxy} - \mu_{void}\right|}{\sigma_{void}} \tag{2}$$

Where μ_{epoxy} is the mean grey value of the epoxy resin calculated between 0 and 32 µm, and μ_{void}contains the mean grey value of the meso-void calculated between 56 and 71 µm of the corresponding line profile from Figure 4. σ_{void} describes the standard deviation of the grey values present in the meso-void.

Figure 5 shows the calculated CNR in correlation to the voxel size. With disabled physical effects (noPE), the CNR is quite constant at a high level between 100 and 250. As soon as physical effects are enabled (+PE) at high resolutions, the CNR is rather low (<10) and increases with reduced resolution.

For evaluation of the edge sharpness of an macro-/mesoscaled void, respectively, to the individual voxel size of $(0.5\ \mu m)^3$, $(2.5\ \mu m)^3$, $(5\ \mu m)^3$ and $(10\ \mu m)^3$, 198, 70, 22 and 4 parallel line profiles were evaluated in Figure 6 to reduce the influence of image noise. Using a minimum change in grey values of 0.1 as lower limit, Figure 6(a) shows a clear trend that high resolution scans deliver higher image sharpness. As soon physical effects are enabled, image sharpness is reduced, and edge blurring is increased significantly. For example, for $(2.5\ \mu m)^3$ voxel size, the edge blurring was increased from ~1 to ~4 µm or for the $(10\ \mu m)^3$ voxel size from ~5 to 11 µm. Looking at sharpness in terms of used

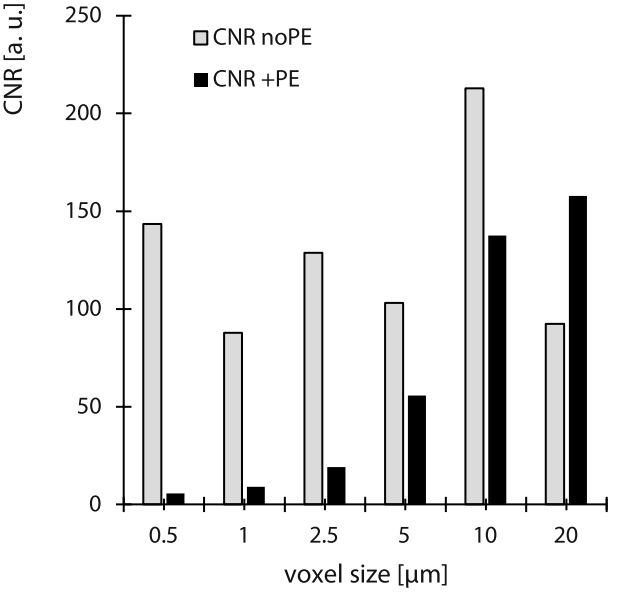

Figure 5. Calculated contrast to noise ratio (CNR) with disabled (noPE) and with enabled physical effects (+PE) at various voxel sizes for the epoxy resin specimen.

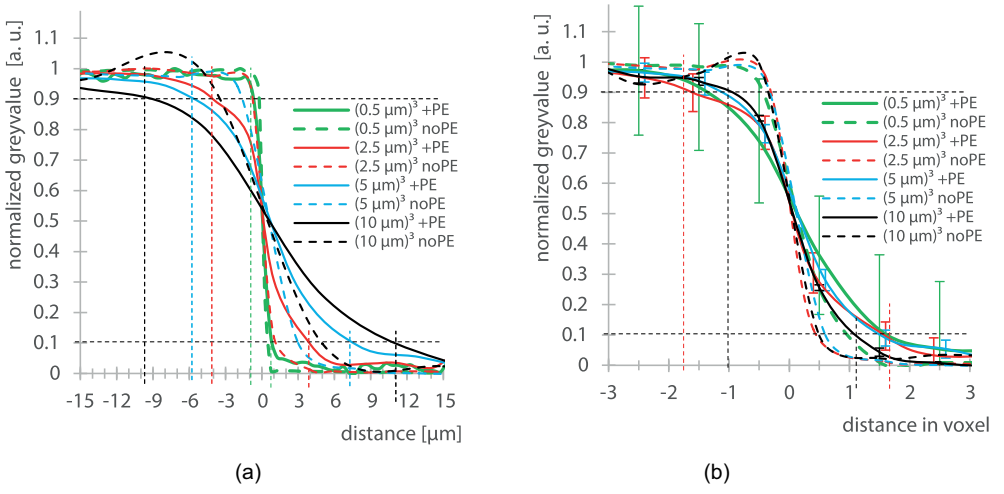

Figure 6. Average grey value profiles showing the edge response of a macro-/mesoscaled void from Figure 3 for evaluation of sharpness and edge blurring.

voxels to detect one edge of a macro-/mesoscaled void in Figure 6(b), it is clearly visible that with non-physical effects, less than 1 voxel would be sufficient. As soon physical effects are enabled, at least 2 voxels are involved for edge detection. Depicted error bars in Figure 6(b) for the +PE graphs show the standard deviation of the grey values on the certain voxel–distance evaluated from the parallel line profiles, representing the image noise discussed in Figure 4.

The observed increase in edge blurring (Figure 6) by enabled physical effects is mainly a result of image blur caused by the scintillator, simultaneously reducing the local image noise (Figure 4) and therefore increases the SNR (Figure 5) at lower resolutions.

3.2. ISO50 threshold for segmentation

In Figure 7, CT simulation results with $(2.5\,\mu m)^3$, $(5\,\mu m)^3$, $(10\,\mu m)^3$, $(20\,\mu m)^3$ and $(40\,\mu m)^3$ voxel sizes are shown for the epoxy resin matrix model. In the bottom row, the void segmentation was done by using an ISO50 threshold for all different resolutions, showing that the segmentation results, especially for the micro-voids, looks good for Figure 7(a) and Figure 7(b) and significantly reduces in Figure 7(c) to Figure 7(d) at lower resolutions.

In Figure 8(a), the calculated void content with ISO50 threshold segmentation shown in Figure 7 is evaluated in three different ROIs of the CT dataset (overall, macro-voids only, micro-voids only) and plotted over the simulated voxel size. It is clearly visible that the evaluated overall void content as well as the porosity evaluated in the micro-void ROI is significantly decreasing at lower resolutions, but nevertheless the void content in the macro-void ROI keeps quite constant up to $(10\,\mu m)^3$ voxel size. In Figure 8(b), the relative deviation from the nominal porosity, calculated from simulation input files, is plotted over the voxel size, showing a significant drop for the overall and micro-voids porosity. The deviation of the segmented macro-voids is quite low in the range of 10% above $(20\,\mu m)^3$ voxel size and close to 0 (c) below $(10\,\mu m)^3$ voxel size.

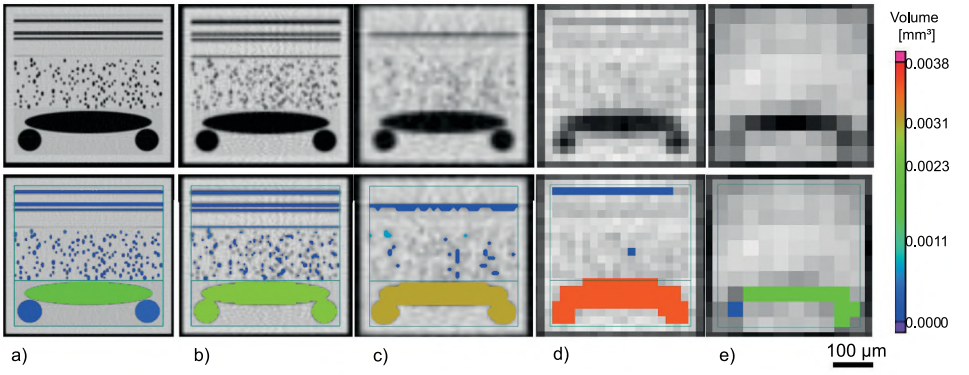

Figure 7. Axial slice image as CT simulation results from reference part (#0) generated with $(2.5\ \mu m)^3$ (a); $(5\ \mu m)^3$ (b); $(10\ \mu m)^3$ (c); $(20\ \mu m)^3$ (d); and $(40\ \mu m)^3$ (e) voxel size and corresponding segmentation results with ISO50 threshold (bottom row). Physical effects were deactivated.

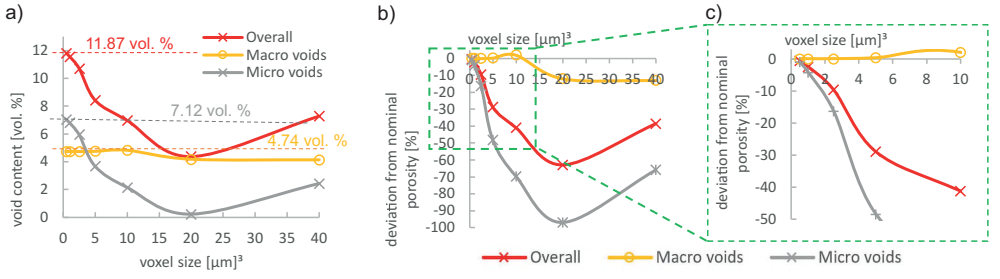

Figure 8. (a) voxel size dependent segmentation result based on an ISO50 threshold segmentation of three different evaluation regions (ROIs) compared to the nominal porosity from simulation input file (dotted lines). (b) and (c) show the relative deviation from the nominal porosity values. Physical effects were deactivated.

3.3. Adapted ISOxx threshold for segmentation

Adapting the global ISOxx threshold to ISO57, ISO63, ISO76 and ISO79 for the samples simulated with $(2.5\ \mu m)^3$, $(5\ \mu m)^3$, $(10\ \mu m)^3$ and $(20\ \mu m)^3$ voxel size shown in Figure 7 would lead to a proper overall void content of 11.87 vol.%. As soon as the resolution is not high enough to avoid partial volume effects, a compromise between over segmentation of the macro-voids and under segmentation of micro-voids has to be made. Enabled physical effects in the simulation tool leads to higher ISOxx threshold values to overcome influence of image noise and edge blurring, as discussed in chapter 3.1. In addition, segmentation parameters such as the minimum considered pore size for segmentation can be a critical value to reduce significantly over-segmentations due to high image noise at high resolution scans. As soon as additional physical effects are enabled, it was observed that for a proper overall void content, the afore mentioned ISOxx threshold values have to be increased to ISO65.8, ISO76.5 or ISO83.95, respectively, for the $(2.5\ \mu m)^3$, $(5\ \mu m)^3$ and $(10\ \mu m)^3$ voxel size resolutions to compensate the reduced sharpness shown in Figure 6.

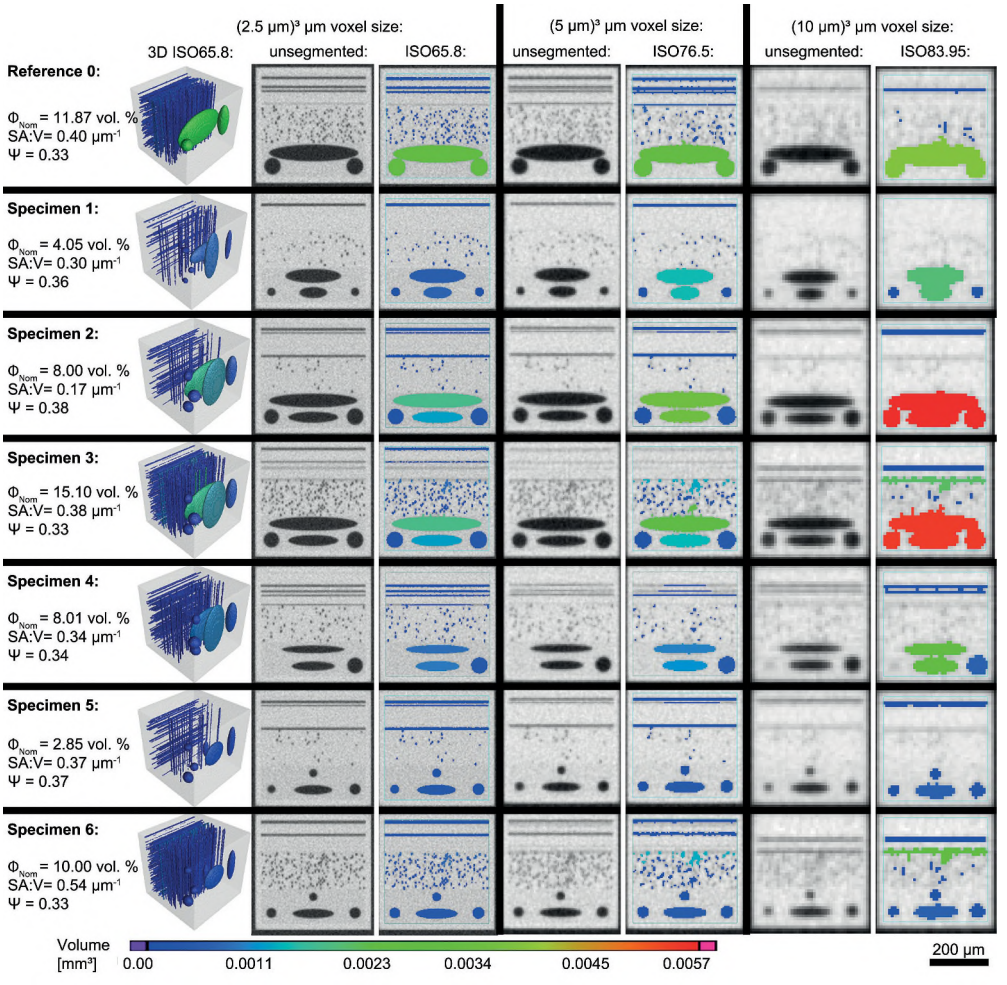

Figure 9. Axial slice image as CT simulation results generated with $(2.5\ \mu m)^3$ (a); $(5\ \mu m)^3$ (b); $(10\ \mu m)^3$ and segmented voids by a determined ISOxx threshold as well as the nominal porosity (φ_{nom}), total surface area to volume ratio (SA/V) and sphericity (ψ). Physical effects were enabled.

To estimate the error of a segmentation with pre-determined ISOxx thresholds ISO65.8, ISO76.5 or ISO83.95 for a certain resolution, additional virtual specimens (#1 to #6) were generated with the CT simulation tool. As shown in Figure 9, the values of total porosity range from 2.85 to 15.1 vol.% and the physical effects were activated. The final segmentation was carried out with ISOxx threshold, delivering a porosity close to nominal porosity for the Reference specimen 0. Figure 9 shows a strong under-segmentation of the micro-voids, which have to be compensated by an over-segmentation of the meso- and macro-voids to deliver porosity values close to nominal input values. This effect increases for lower resolutions as seen for the $(10\ \mu m)^3$ simulations.

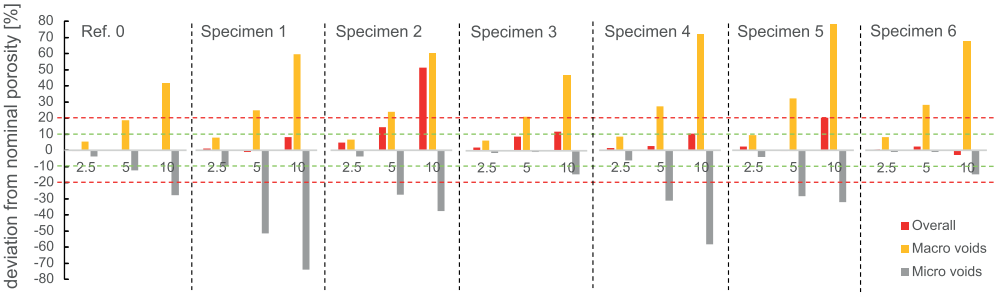

Figure 10. Relative deviation from nominal porosity values of the individual specimens 0 to 6 and three different evaluation ROIs. Dashed green and red line shows the boundaries for 10% and 20% deviation error, respectively. Physical effects were enabled.

In Figure 10, the relative deviation to the nominal porosity of the individual datasets segmented by an ISOxx value and certain ROIs is shown. For "Ref.0" data, the overall deviation is 0% because this one was used for calibrating the proper ISOxx value. Only a clear under-segmentation of the micro-voids and over-segmentation of the macro-voids is visible. Looking to the ISO65.8 segmentation results of the (2.5 µm) simulations of all specimens, it is clearly visible that the deviation of overall porosity is close to zero for all of them. Comparing the segmentation results using an ISO76.5 threshold for the $(5\ \mu m)^3$ simulations, only Specimen 2 shows deviation larger +10% compared to its nominal porosity of 8.0 vol.%. Looking at the overall porosity deviations from the $(10\ \mu m)^3$ simulations segmented with an ISO83.95 threshold shows still deviations smaller +10% for specimen 1, 3, 4 and 6 as well as smaller +20 % for Specimen 5. Specimen 2 has a large deviation of overall porosity in the range of +50%. Referencing back to Figure 10 may explain this high deviation for specimen 2 because the amount of micro- and macro-voids greatly deviates from the Reference sample 0, which was used for ISOxx calibration. This strong deviation can also be described with a quantitative value by using the ratio of the total surface area (SA) divided by the total volume (V) of the voids within a specimen. The SA/V ratio of 0.33 μm^{-1} for Ref. 0 differs greatly from Specimen 2 with a value of 0.17 μm^{-1}. The other specimens have a SA/V ratio close to Ref. 0 sample as well less deviation in total porosity.

Calculating a mean error of the overall porosity (specimen 1–6) using the ISOxx segmentation method results in a relative deviation of 1.95%, 4.65% and 16.58% for the simulations performed with $(2.5\ \mu m)^3$, $(5\ \mu m)^3$ and $(10\ \mu m)^3$ voxel size, respectively. Neglecting specimen 2 from this results, relative deviations would be at 1.4%, 2.7% and 9.65% for the abovementioned resolutions.

3.4. Correlation of surface to volume ratio to segmentation errors

To investigate the influence of the SA/V ratio on the segmentation results of simulated CT data, a set of 13 different meso- and macro-voids (ID0 to ID12) were simulated at $(5\ \mu m)^3$, $(10\ \mu m)^3$ and $(20\ \mu m)^3$ voxel size with enabled physical effects, as shown in Figure 11. The segmentation was done with an ISO50 threshold for all the specimens, and in addition, an individual ISOxx value was determined for each set and resolution to reach the nominal porosity given by the simulation input file. The pores were modelled in such

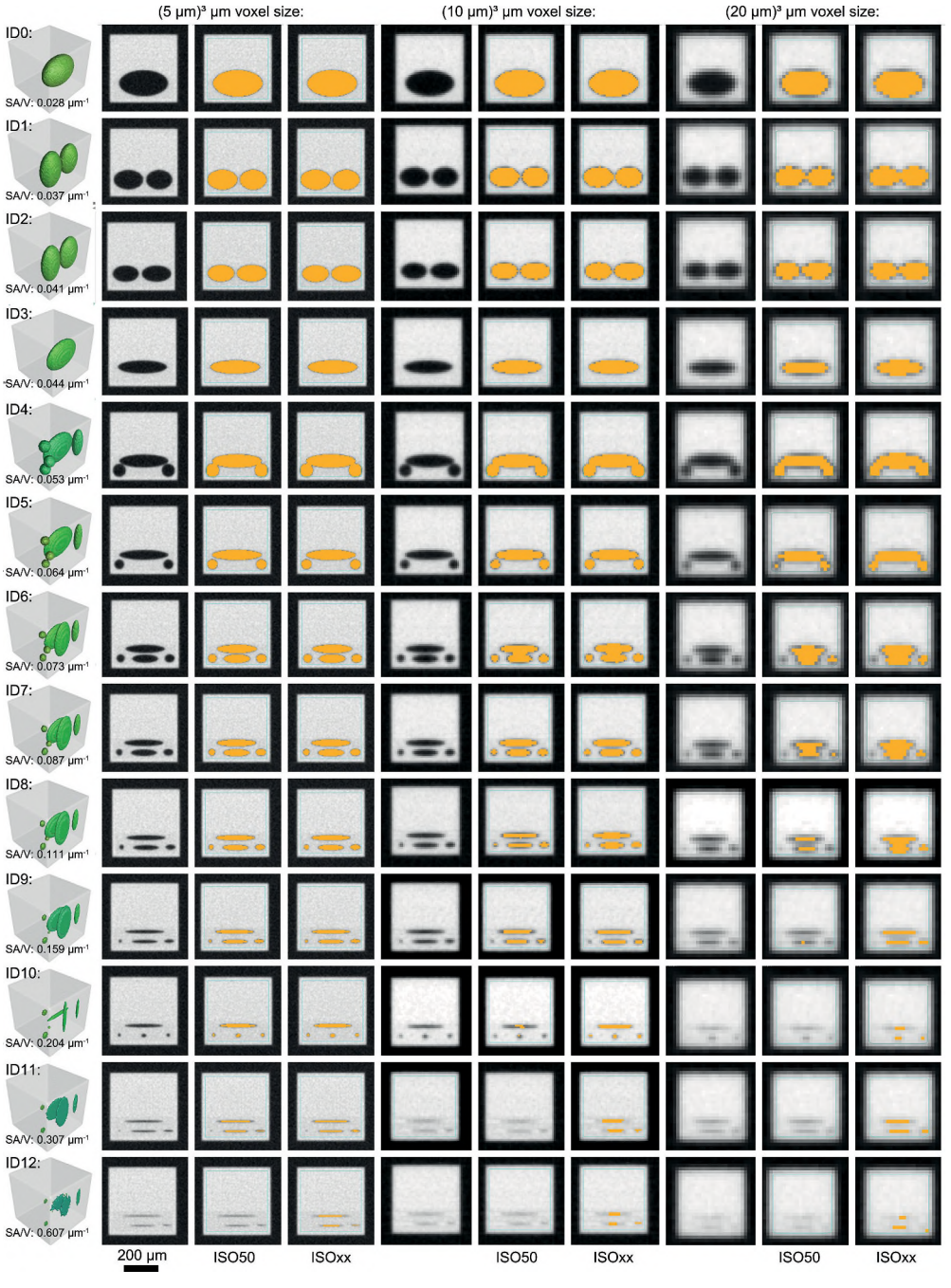

Figure 11. Set of different objects to investigate the influence of the SA/V ratio on the segmentation results of simulated CT data at $(5\ \mu m)^3$, $(10\ \mu m)^3$ and $(20\ \mu m)^3$. Physical effects were enabled.

a way that the minimum diameter (D) of the individual objects was reduced in certain steps from 160 µm (ID0) to 5 µm (ID12). Other dimensions of the objects were larger, so a broad variation of different SA/V ratios was possible.

In Figure 12, the correlations between different global form factors calculated from sample ID0 to ID12 from Figure 11 on the relative segmentation error using an ISO50 threshold at different voxel resolutions are depicted. Beside the SA/V ratio, a spherical equivalent diameter (d_V) is calculated from the total nominal void volume (V_{voids}) in Equation (3) as well as the sphericity (ψ) defined by Wadell [22] in Equation (4) as a quadratic ratio of (d_V) and an equivalent diameter (d_{SA}) from the surface area (SA) of an object (Equation (5)).

$$d_V = \sqrt[3]{\frac{6 * V_{voids}}{\pi}} \tag{3}$$

$$\psi = \frac{{d_V}^2}{{d_{SA}}^2} \tag{4}$$

$$d_{SA} = \sqrt{\frac{4 * SA}{\pi}} \tag{5}$$

Comparing these three shape factors, in Figure 12(a) the SA/V ratio shows a linear correlation to the relative segmentation error using an ISO50 threshold with a coefficient of determination (R^2) higher than 0.93 for all resolutions. Compared to SA/V ratio, the correlation of the calculated sphericity in Figure 12(b) to a logarithmic fit is much lower. Another drawback using sphericity to describe voids is that this form factor has no unit, so there is no difference between a large spherical void and a small spherical void. Both will have the value "1". For the volume equivalent diameter (d_V), no suitable correlation could be found in Figure 12(c) in these investigations.

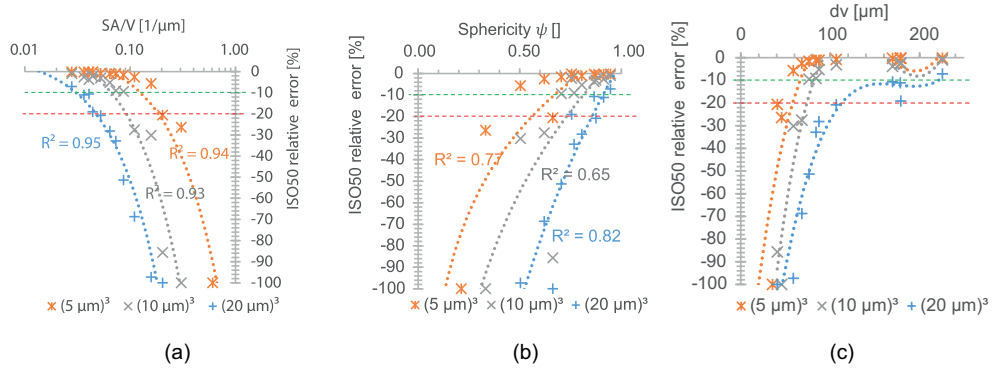

Figure 12. Correlation between global variables SA/V (a); sphericity ψ (b) and spherical equivalent diameter(d_V)(c) calculated from sample ID0 to ID12 from Figure 11 on the relative segmentation error using an ISO50 threshold at different voxel resolutions.

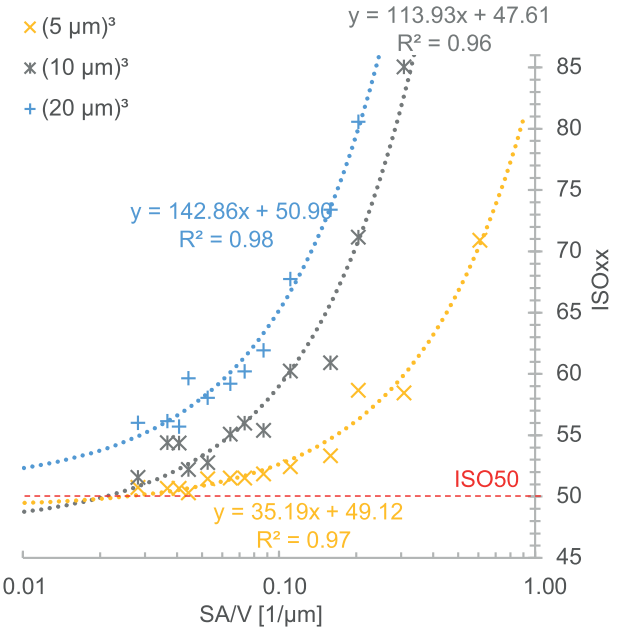

Figure 13. Correlation between SA/V ratio and the proper ISOxx threshold for correct segmentation results at a certain voxel size.

In Figure 13, the SA/V ratio is depicted against the proper ISOxx threshold for determining the correct porosity given by the nominal input file of the simulation data. The graph shows a strong linear correlation, with an R^2 higher than 0.96 for all investigated resolutions.

3.5. Spherical equivalent diameter from SA/V ratio

The fact that the SA/V ratio has a unit of 1/µm gives us the possibility to calculate an equivalent diameter ($d_{SA/V}$) according to Equation (6) below:

$$\frac{\mathbf{SA_{voids}}}{\mathbf{V_{voids}}} = \frac{\pi * \mathbf{d^2}}{\frac{1}{6} * \pi * \mathbf{d^3}} \rightarrow \mathbf{d_{SA/V}} = \mathbf{6} * \left(\frac{\mathbf{V_{voids}}}{\mathbf{SA_{voids}}}\right) \tag{6}$$

In Figure 14, several sphere equivalent diameters (d) calculated from the surface area (d_{SA}), the volume (d_V) and the SA/V ratio ($d_{SA/V}$) are plotted together with the minimal diameter (min D) which was used as manual input to generate the individual objects in ID0-ID12. This diagram shows, especially for ID11 & 12, a much closer approach of $d_{SA/V}$ to the critical minimal diameter for segmentation, unlike to (d_V) or (d_{SA}) showing quite high values. Also, at larger diameters (e.g. ID3), the dSA/V value is more stable and trending to values closer to the minimal diameters.

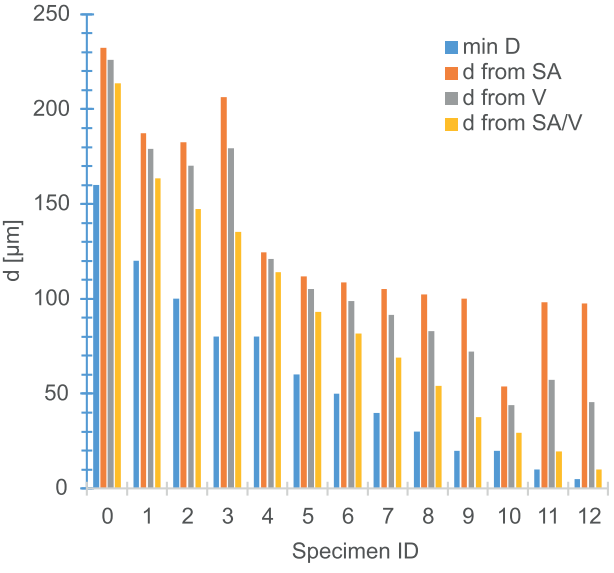

Figure 14. Sphere equivalent diameters (d) calculated from surface area (SA), volume (V) and SA/V ratio are plotted together with a minimal pore diameter (min D) defined as simulation input.

3.6. Estimation of a minimal voxel size

As already discussed in Figure 6, at least two voxels are involved to represent one edge of a void, so the third voxel in a row is the first one representing the volume 100% correct. Same behaviour occurs on the second edge, back to the matrix. This leads us to the assumption that at least six voxels in a row are necessary to segment the correct volume of an object. In addition, when all kinds of physical effects are neglected, the edges of an object (e.g. cylinder with 3 µm diameter in a $(1\ \mu m)^3$ voxel grid) can be located exactly on the boundary of two voxels or somewhere between as shown in Figure 15. In dependence on these positions, with an ISO50 threshold, all grey values <0.5 will be segmented as void voxel. Based on both extreme positions, 2D segmentation area of the same cylinder can result in a minimum of 2 × 2 voxels or a maximum of 3 × 3 voxel. From this, a minimum and a maximum mean segmentation area in the 2D image of 6.5 μm^2 can be calculated, which is −8% below the theoretical cylindrical area of 7.068 μm^2.

Using this assumption, which is below 10% error, a potential minimal voxel size can be calculated from the $d_{SA/V}$. This expected minimal voxel size $VS_{min} = 1/6^{*}d_{SA/V}$ is depicted in Table 1, together with several other calculated values as well as the relative segmentation errors already presented in Figure 12. Comparing the expected VS_{min} to the relative segmentation errors, there is a strong correlation. As soon as the expected VS_{min} does not fit to the $(5\ \mu m)^3$, $(10\ \mu m)^3$ or $(20\ \mu m)^3$ simulations, the relative error exceeds a value of +10%. For ID 0–2, all resolutions deliver a small error in the range of <10%, and for ID 10 to 12, a voxel size below $(5\ \mu m)^3$ would be essential to reduce the segmentation error using an ISO50 threshold.

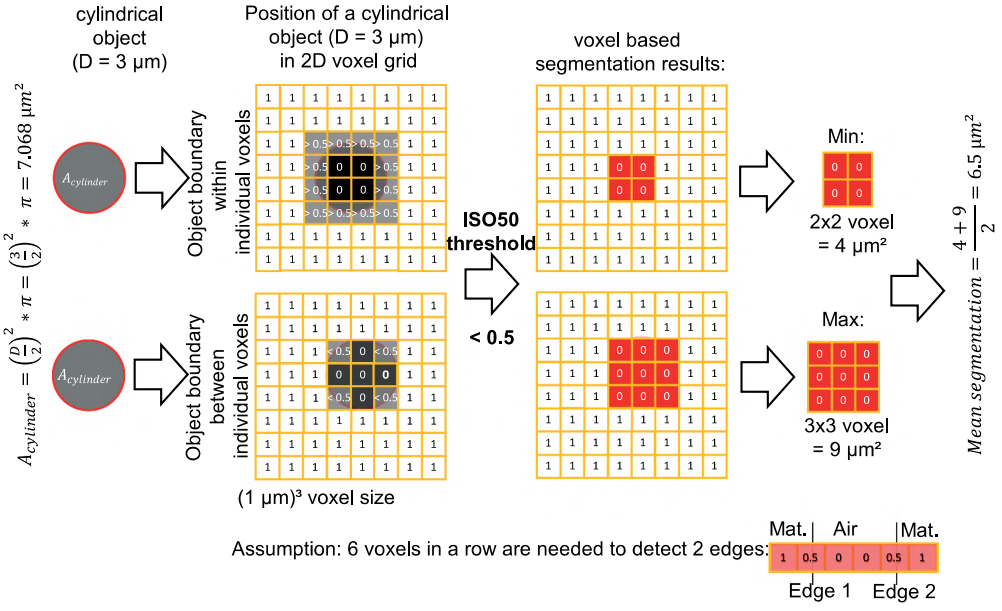

Figure 15. 2D slice of a cylindrical object with 3 µm in diameter, leading to different segmentation results on dependence of exact position in the 1 µm voxel grid. These schematic results were used to estimate an average segmentation error using six voxels in a row for object segmentation.

Table 1. Minimal voxel size (Vs_{min}) calculated from $d_{sa/v}$ required for correct ISO50 segmentation with less than 10% error and compared with relative errors from simulations done with (5 µm)³, (10 µm)³ and (20 µm)³ voxel size (VS), respectively.

		Calculated from nominal input values				ISO50 porosity segmentation Relative error [%]		
Specimen ID	Min. D [µm]	Nominal porosity [vol.%]	SA/V [1/µm]	$d_{SA/V}$ [µm]	VS_{min} [µm]	VS (5 µm)³	VS (10 µm)³	VS (20 µm)³
0	160	11.44	0.028	213.67	35.61	*−0.19*	*−0.98*	*−7.12*
1	120	11.39	0.037	163.67	27.28	*−0.28*	*−2.67*	*−11.13*
2	100	9.77	0.041	147.40	24.57	*−0.26*	*−3.79*	*−10.67*
3	80	5.72	0.044	135.37	22.56	*−0.19*	*−2.25*	−19.06
4	80	8.77	0.053	114.05	19.01	*−0.79*	*−3.13*	−20.77
5	60	5.79	0.064	93.10	15.52	*−1.09*	*−5.26*	−28.16
6	50	5.76	0.073	81.80	13.63	*−1.04*	*−9.07*	−32.83
7	40	4.55	0.087	68.91	11.49	*−1.61*	*−9.43*	−51.32
8	30	3.39	0.111	54.26	9.04	*−2.56*	−27.59	−68.69
9	20	2.25	0.159	37.76	6.29	*−5.69*	−30.20	−97.29
10	20	0.51	0.204	29.43	4.91	−20.60	−85.67	−100.00
11	10	1.12	0.307	19.53	3.26	−26.40	−100.00	−100.00
12	5	0.56	0.607	9.88	1.65	−100.00	−100.00	−100.00

3.7. Variation of matrix material

For this simulation study, three different matrix materials were investigated. The first was a typical epoxy resin combination with a density of 1.36 g/cm³ described by the following chemical formula as input for simulation: C11H12O3. In practical use,

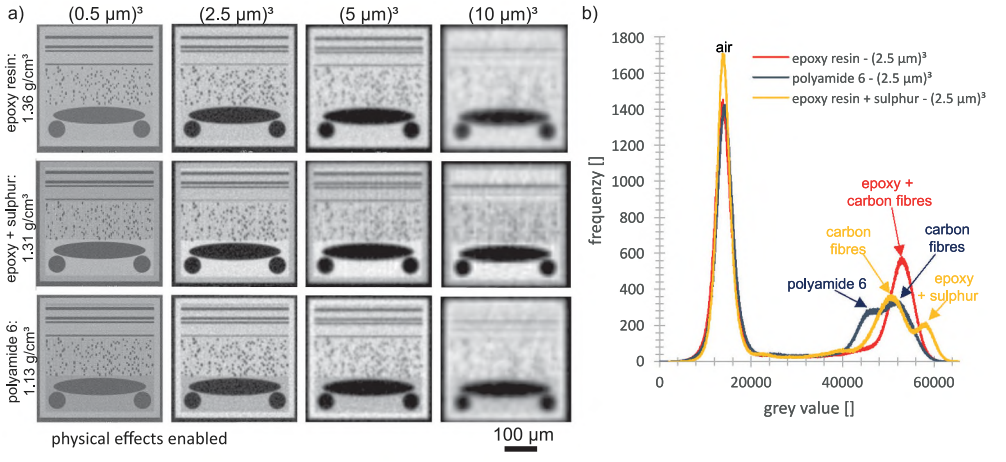

Figure 16. (a) CT-simulation slice images performed at (0.5 µm)^3 to (10 µm)^3 voxel size and varying polymer matrix systems with different densities and absorption coefficients. (b) Grey value histograms of these material combinations at a resolution of (2.5 µm)^3 voxel size. Physical effects were enabled.

epoxy resin combinations with higher absorption contrast are also available [23]. Separate energy dispersive X-ray analysis (EDX) on parts like this has shown that some sulphur is added to the epoxy. This was also done in our study by adding 0.05% of sulphur as simulation input for our second matrix material combination. The density itself was reduced slightly to 1.31 g/cm^3 according to material datasheets. Finally, matrix material polyamide 6 with 1.13 g/cm^3 was modelled by the following chemical formula: C6H11NO. In Figure 16(a), the simulation results of all combinations are depicted. In Figure 16(b), the grey value histograms of these material combinations including individual carbon fibres at a resolution of (2.5 µm)^3 voxel size are shown, depicting completely different material peaks. Choosing a wrong material peak for threshold calculation may lead to wrong segmentation results. So for new material systems, it is of high importance that a separate ISOxx threshold is adjusted before doing quantitative analysis. In our studies, with ISO50 segmentation, best results were achieved when using the carbon fibre peak for polyamide 6 and the epoxy–sulphur peak. Both have the effect of maximising the contrast between air and material. It has to be noted that, especially for polyamide, it can easily come to over-segmentations in the matrix area due to noise. To reduce this effect, especially for higher resolutions, the minimal segmented voxel/defect size has to be increased for quantitative porosity determination.

4. Conclusion

This work presents a CT simulation study in which microstructures such as individual carbon fibres, micro-voids and the polymer matrix including mesoscale voids were taken into account to generate virtual CT data with well-known porosity. By analysing these synthetically generated datasets, it was shown that the presence of microstructure-like

needle-like micro-voids and the individual carbon fibres have a big influence on the segmentation results. Therefore, these structures have to be modelled or taken into account in CT simulation studies of fibre-reinforced polymers. Even this will affect the calculation time enormously. Furthermore, it was shown that a simple ISO50 threshold is suitable for reliable quantitative segmentation results of voids, as long as the resolution is high enough. With this knowledge, applied multiscale approaches [24] for new materials as carried out for example in [10,25–27] are meaningful and very important. As soon as one reference porosity value of a certain volume can be determined by this approach, it is possible to use an adapted ISOxx threshold to investigate a larger sample volume at lower resolutions.

The accuracy of an ISO50 threshold strongly depends on the final resolution and the size and shape of the voids within the material. To describe them, the ratio of total surface area (SA) divided by the total volume (V) of the voids (SA/V) seem to be a very promising value which enables the calculation of a minimal voxel size needed to enable a reliable segmentation of voids by a simple ISO50 threshold below a relative error of 10%.

As soon as a proper ISOxx threshold was determined and applied to six different specimens, the relative error of total void content was below 2% for the $(2.5\ \mu m)^3$, below 5% for the $(5\ \mu m)^3$ and below 17% for the $(10\ \mu m)^3$ voxel size simulations as depicted in Figure 10. As noted before, the SA/V ratio of voids within a specimen plays an important role. If this value differs a lot between the individual samples, then the measurement error is increased, as seen for Specimen 2 in Figure 10. By ignoring the results from Specimen 2, because the SA/V ratio was at $0.17\ \mu m^{-1}$ instead of $0.4\ \mu m^{-1}$ from the reference part, for the remaining five specimens, a relative error of less than 3% for the $(5\ \mu m)^3$ and less than 10% for $(10\ \mu m)^3$ simulations was determined. In addition, it should be noted that in real CT scans, propagation-based phase contrast effects also occur [20,24], which can significantly increase the visibility of micro-voids with certain CT systems, resulting in lower ISOxx threshold values.

This study has also demonstrated that as soon as something changes within the sample, e.g.: completely different void morphology due to another manufacturing process or by using different polymers or adding some additives as well when additional artefacts are induced or CT parameters or the CT system is changed, a new calibration of the ISOxx values has to be done.

Finally, to sum up, using an easy-to-apply ISOxx threshold delivers good results for quantitative porosity results even at voxel sizes above resolving all microstructures. A global threshold is always a trade-off between over-segmentation of macropores and under-segmentation of micropores. CT is a reliable method for quantitative porosity determination and can be competitive at least with current standard procedures such as acid digestions or microscopy where accuracy is in the range of ±1.0 vol.%, with the great benefit that CT is non-destructive. This means that in addition to the complete 3D information of a given volume, the same samples can also be further investigated with other methods to better interpret unclear results or to use them as reference parts for other non-destructive [6] or destructive methods [28].

This study has also shown that very high resolution is required for the accurate extraction of void microstructures needed for, e.g. finite element simulations [29,30]. For this purpose, a minimum voxel size can be estimated from the SA/V ratio to plan the required CT scans.

To sum up and as an outlook, using the concept of SA/V ratio descript in this work should also be usable on real CT data for following purposes:

- For quality control of porosity analysis. When SA/V ratio is very similar, same ISOxx threshold values can be applied for quantitative porosity evaluations, assuming the same material system, CT device and measurement parameters.
- To proof if resolution is high enough to use an ISO50 threshold to determine a reference porosity or extracting real microstructure geometries.
- To estimate the proper ISOxx threshold for lower resolution scans based on diagrams shown in Figure 13.
- To create a material database of porous materials described in addition with the SA/V ratio. Then the decision between choosing an already determined ISOxx threshold or performing a new, time-consuming ISOxx calibration procedure can be made.
- SA/V ratio should also work for other microstructures, such as fibres, to make a decision which resolution is necessary for a voxel-based segmentation and feature extraction.

Acknowledgments

This work is part of the research projects 'BeyondInspection' (grant number 874540) and 'pore3D' (grant number 868735) funded by the Austrian Research Promotion Agency (FFG) and the state government of Upper Austria. We would also like to thank Peter Orgill from University of Applied Sciences Upper Austria for proofreading.

Disclosure statement

No potential conflict of interest was reported by the author(s).

Funding

The work was supported by the österreichische Forschungsförderungsgesellschaft [874540, 868735].

ORCID

Bernhard Plank http://orcid.org/0000-0003-4430-9352
Markus G. R. Sause http://orcid.org/0000-0002-6477-0691
Johann Kastner http://orcid.org/0000-0002-3163-0916

References

[1] Bossi RH. Non destructive evaluation developments for composite structures. Am Inst Phys Conf Proc. 2005;820:965–971.
[2] Helmus R. Out-of-Autoclave Prepregs: Stochastic Modelling of Void Formation [PhD at Technische Universität München]. 2016: pp. 159.
[3] Längauer M, Zitzenbacher G, Heupl S, et al. Influence of thermal deconsolidation on the anisotropic thermal conductivity of glass fiber reinforced, pre-consolidated polypropylene sheets used for thermoforming applications. Polym Composites. 2022;43(4):2264–2275. DOI:10.1002/pc.26538

[4] Shi H, Villegas IF, Bersee HE. Analysis of void formation in thermoplastic composites during resistance welding. J Thermoplast Composite Mater. 2017;30(12):1654–1674.
[5] Stamopoulos A, Tserpes K, Prucha P, et al. Evaluation of porosity effects on the mechanical properties of carbon fiber-reinforced plastic unidirectional laminates by X-ray computed tomography and mechanical testing. J Compos Mater. 2015;50(15):12.
[6] Mayr G, Plank B, Sekelja J, et al. Active thermography as a quantitative method for non-destructive evaluation of porous carbon fiber reinforced polymers. NDT & E International. 2011;44(7):537–543. DOI:10.1016/j.ndteint.2011.05.012
[7] Yolken HT, Matzkanin GA, Bartel JE. Nondestructive evaluation (NDE) of advanced fiber reinforced polymer composites. Austin (TX): Nondestructive Testing Information Analysis Center; 2002. (Report no. NTIAC-TA-01-01, Contract no. SPO700-97-D-4003, Sponsored by the Department of Defense).
[8] Costa ML, Almeida SFM, Rezende MC. The influence of porosity on the interlaminar shear strength of carbon/epoxy and carbon/bismaleimide fabric laminates. Compos Sci Technol. 2001;61(14):2101–2108.
[9] Birt EA, Smith RA. A review of NDE methods for porosity measurement in fibre-reinforced polymer composites. Insight. 2004;46(11):681–686.
[10] Khudiakova A, Berer M, Niedermair S, et al. Systematic analysis of the mechanical anisotropy of fibre-reinforced polymer specimens produced by laser sintering. Additive Manuf. 2020;36:101671.
[11] Terekhina S, Tarasova T, Egorov S, et al. The effect of build orientation on both flexural quasi-static and fatigue behaviours of filament deposited PA6 polymer. Int J Fatigue. 2020;140:105825.
[12] Kiefel D. Quantitative Porositätscharakterisierung von CFK-Werkstoffen mit der Mikro-Computertomografie [dissertation]. Munich (Germany): Technische Universität München; 2017: 207.
[13] Plank B, Rao G, Kastner J. Evaluation of CFRP-reference samples for porosity made by drilling and comparison with industrial porosity samples by means of quantitative X-ray computed tomography. Proceedings of the 7th International Symposium on NDT in Aerospace; 2015; Bremen, Germany. p. 10.
[14] Kastner J, Plank B, Salaberger D, et al. Defect and porosity determination of fibre reinforced polymers by X-ray computed tomography. Proceedings of 2nd International Symposium on NDT in Aerospace; 2010; Hamburg, Germany. p. 12.
[15] Reiter M, Gusenbauer C, Huemer R, et al. At-Line X-ray computed tomography of serial parts optimized by numerical simulations. Proceedings of Symposium on Digital Industrial Radiology and Computed Tomography (DIR2019); 2019; Fürth, Germany. p. 9.
[16] Kiefel D, Stössel R, Plank B, et al. CFRP porosity characterisation using μ-computed tomography with optimized test parameters supported by XCT-simulation. Proceedings of Conference on Industrial Computed Tomography (iCT2014); 2014; Wels, Austria. p. 35–43.
[17] Tretiak I, Smith RA. A parametric study of segmentation thresholds for X-ray CT porosity characterisation in composite materials. Compos Part a Appl Sci Manuf. 2019;123:10–24.
[18] Reiter M, Erler M, Kuhn C, et al. SimCT: a simulation tool for X-ray imaging, Proceedings of Conference on Industrial Computed Tomography (iCT2016); 2016; Wels, Austria. p. 7.
[19] Gusenbauer C, Reiter M, Salaberger D, et al. Simulation-Based optimization of nano-XCT scans for high-resolution applications. Proceedings of the 8th Conference on Industrial Computed Tomography (iCT2018); 2018; Wels, Austria. p. 8.
[20] Kastner J, Plank B, Requena G. Non-Destructive characterisation of polymers and al-alloys by polychromatic cone-beam phase contrast tomography. Mater Charact. 2012;64:79–87.
[21] ISO 15708-3. Nondestructive testing - radiation methods - computed tomography - part 3: operation and interpretation. 2017.
[22] Wadell H. Shape, and roundness of quartz particles. J Geol. 1935;43(3):250–280.

[23] Revol V, Plank B, Kaufmann R, et al. Laminate fibre structure characterisation of carbon fibre-reinforced polymers by X-ray scatter dark field imaging with a grating interferometer. NDT E Int. 2013;58:64–71.
[24] Plank B, Schiwarth M, Senck S, et al. Multiscale and multimodal approaches for three dimensional materials characterisation of fibre reinforced polymers by means of X-ray based NDT methods. Proceedings of Symposium on Digital Industrial Radiology and Computed Tomography (DIR2019); 2019; Fürth, Germany. p. 11.
[25] Stelzer PS, Plank B, Major Z. Mesostructural simulation of discontinuous prepreg platelet based carbon fibre sheet moulding compounds informed by X-ray Computed Tomography. Case Stud NondestrTest Eval. 2020;35(3):342–358.
[26] Savandaiah C, Plank B, Maurer J, et al. Comparative study of filled and unfilled polylactic acid produced via injection molding and 3D printing. In SPE ANTEC®Classic, Proceedings of the Plastic Technology Conference, Virtual - Online; 2021; p. 9.
[27] Senck S, Happl M, Reiter M, et al. Additive manufacturing and non-destructive testing of topology-optimised aluminium components. Case Stud NondestrTest Eval. 2020;35(3):315–327. DOI:10.1080/10589759.2020.1774582
[28] Stadler H, Kiss P, Stadlbauer W, et al. Influence of consolidating process on the properties of composites from thermosetting carbon fibre reinforced tapes. Polym Composites. 2022. in press. DOI:10.1002/pc.26687.
[29] Czabaj MW, Riccio ML, Whitacre WW. Numerical reconstruction of graphite/epoxy composite microstructure based on sub-micron resolution X-ray computed tomography. Compos Sci Technol. 2014;105:174–182.
[30] Scott AE, Sinclair I, Spearing SM, et al. Influence of voids on damage mechanisms in carbon/epoxy composites determined via high resolution computed tomography. Compos Sci Technol. 2014;90:147–153.